

Terahertz Hybrid Topological Chip for 10-Gbps Full-Duplex Communications

Haisu Li ^{1,*} , Yu Zhang ¹, Yajing Liu ¹ and Shaghik Atakaramians ²

¹ Key Laboratory of All Optical Network and Advanced Telecommunication Network of EMC, Institute of Lightwave Technology, Beijing Jiaotong University, Beijing 100044, China

² Terahertz Innovation Group, School of Electrical Engineering and Telecommunications, UNSW Sydney, Sydney, NSW 2052, Australia

* Correspondence: lihaisu@bjtu.edu.cn

Abstract: Terahertz photonic chips play an important role in next-generation information systems, such as high-speed inter/intrachip connections. Here we report a hybrid hollow-core terahertz topological planar waveguide where topological silicon pillars (assembled as expanded and compressed hexagonal clusters) are sandwiched between parallel gold plates. Assisted by numerical optimization of topological waveguide unit cells and supercells, we achieve a wide topological bandgap (relative bandwidth of 16.1%) in which two low-loss (below 0.1 dB/mm) topological pseudospin states exist and cover 81.8% of the bandgap. The dual unidirectional channel in a single waveguide path can be used for short-range (below 100 mm) 10-Gbps full-duplex on-chip transmissions under the forward error correction limit (bit error rate less than 10^{-3}). Simulation results reveal that the communication performance of the proposed topological waveguide is largely group velocity dispersion dependent. This work may pave an avenue for high-speed integrated circuit design and applications in both electric and photonic fields.

Keywords: terahertz waveguides; topological photonics; terahertz communications; hybrid structures; hollow core



Citation: Li, H.; Zhang, Y.; Liu, Y.; Atakaramians, S. Terahertz Hybrid Topological Chip for 10-Gbps Full-Duplex Communications. *Electronics* **2023**, *12*, 109. <https://doi.org/10.3390/electronics12010109>

Academic Editor: Hector E. Nistazakis

Received: 29 November 2022

Revised: 21 December 2022

Accepted: 26 December 2022

Published: 27 December 2022



Copyright: © 2022 by the authors. Licensee MDPI, Basel, Switzerland. This article is an open access article distributed under the terms and conditions of the Creative Commons Attribution (CC BY) license (<https://creativecommons.org/licenses/by/4.0/>).

1. Introduction

Terahertz radiation has been considered a promising frequency range that could support high-speed transmission applications, such as next-generation communication systems (also known as the 6G) and inter/intra-chip connections (i.e., last-centimeter communication) [1–3]. In contrast to microwave communication technologies, terahertz transmission devices feature a higher carrier frequency, a reduced size, and, the exciting potential to bridge state-of-the-art electric and photonic components [4]. In addition, terahertz waveguides with densely integrated functionalities are able to not only carry and manipulate massive data but also enhance the robustness and compactness of terahertz information systems [5,6]. As a result, many terahertz waveguides inspired by both microwave and photonic regimes have been investigated and demonstrated [7–9]. Specifically, benefiting from the high transparency of high-resistivity silicon in the terahertz range and the well-established microfabrication techniques of silicon wafers, silicon-based planar waveguides are high-quality platforms for short-length (generally a few centimeters) on-chip terahertz communications [10]. A simple example is the silicon-on-insulator waveguide which is uncladded along the lateral direction; in other words, terahertz waves are confined by total internal reflection between the core–air interface, leading to weak mechanical stability and high scattering losses [11]. To solve these issues, microstructured photonic claddings are designed for achieving full-direction confined, self-supporting terahertz photonic integrated chips. In 2015, a terahertz silicon planar waveguide with photonic crystal cladding was reported followed by a great number of works on such a platform, for instance, the integration of passive and active components and on-chip communications [12–15]. Nevertheless,

photonic crystal waveguides suffer from significant losses at sharp corners and unexpected defects. Thanks to the recent advances in 2D topological photonics [16,17], topological waveguides have unprecedented advantages of robust and reflection-free propagations, therefore, attracting huge attention in the terahertz field [18].

Current terahertz topological waveguides largely mimic the quantum spin Hall effect or the quantum valley Hall effect originating from the condensed matter physics field [19,20]. For each class, two pioneering waveguides working at the terahertz regime have been demonstrated in the last two years. Similar to the previous silicon photonic crystal slab, topological propagation was achieved by etching a 2D hexagonal lattice of triangular air holes with two different sizes and opposite orientations in a silicon slab so as to introduce a bandgap of valley photonic crystals. The silicon topological waveguide has low losses below 0.1 dB for a 120° bend [21,22]. Based on this platform, on-chip high-speed communications (up to 108 Gbps) assisted by 16-ary quadrature amplitude modulation were realized [23]. However, the narrow bandgap of the silicon topological waveguide (relative bandwidth of 7.8%) could be a limitation for broadband terahertz communications. To broaden the topological transmission window, our group proposes a hollow-core metallic topological waveguide with tilted pillars which mimics the quantum spin Hall effect [24]. Such a metallic waveguide is fabricated using a fast, cost-effective 3D printer and gold sputtering. Although the relative topological bandgap of the metallic waveguide has a 60% improvement compared to the silicon counterpart, the topological transmission bandwidth is still limited (relative value of 12.5%) [24]. Due to the remarkable properties of topologically protected propagations, numerous waveguide-integrated topological devices have emerged rapidly, including the topological on/off switch, beam splitter, cavity, and sensor amongst others [25–30].

To fully utilize the broad terahertz frequency band, enhancing the topological bandgap is vital for high-speed, high-spectral-efficiency on-chip communications. In this work, we propose a hybrid hollow-core topological waveguide structure consisting of parallel metallic plates and a silicon topological insulator. The optimized waveguide exhibits topological transmissions over 0.278–0.289 THz and 0.242–0.267 THz for two low-loss (below 0.1 dB/mm) unidirectional modes in a single path. Furthermore, we explore the on-chip 10-Gbps full-duplex communication applications of the proposed waveguide.

2. Waveguide Design

The proposed hybrid hollow-core topological waveguide comprises silicon pillars sandwiched between two parallel gold plates. Such a hybrid structure can be realized by exploiting the multiwafer silicon-based fabrication process, which we have developed for fabricating a similar terahertz chip—a hybrid photonic crystal hollow-core waveguide [31]. During the microfabrication process, a 200 μm gold layer was deposited on silicon wafers that was thicker than the skin depths (143–175 nm) of the gold over 0.2–0.3 THz. Throughout this work, the refractive index of high-resistivity silicon was fixed at 3.418, and the complex dielectric constant of gold is expressed using its Drude model, which is the same as our previous work [31].

We start the waveguide design from a honeycomb-latticed unit cell where six silicon pillars formed a hexagonal cluster. The parameters are defined in Figure 1a, where Λ is the lattice constant, d is the distance between the pillar and the honeycomb center, and r is the pillar radius. Keeping the C_6 symmetry invariant, the six-pillar cluster is either expanded or compressed (see Figure 1a where the dashed circles represent the original position of six pillars) to open up a topological bandgap at the Γ point in the Brillouin zone, as shown in Figure 1b. Such deformation led to a pseudospin degree of freedom in the electromagnetic system that is similar to the quantum spin Hall effect [32,33]. To achieve the bandgap appearing at the target transmission band over 0.25–0.3 THz, Λ was determined to be 530 μm. To further explore the possibility of improving the topological bandgap bandwidth, we investigated the influences of d and r on the relative bandwidth using finite element method models of the unit cell where period boundary conditions

were applied to simulate an infinite 2D unit cell array. For more details on finite element method-assisted topological band simulations, please see Ref. [34]. From the results shown in Figure 1c, the relative bandwidth of the topological bandgap was strongly governed by the cluster deformation (i.e., d/Λ) but less affected by the relative pillar dimension (i.e., r/Λ). We should note here that the maximum possible bandwidth was limited by both d and r since the cluster cannot be excessively expanded or compressed; meanwhile, the pillars should not be oversized in order to avoid adjacent pillars touching each other. Therefore, d and r values were, respectively, selected to be 0.375 (0.278) Λ and 0.111 Λ for a relative bandwidth of 16.1% (0.256–0.3 THz, i.e., the crossings between the dashed horizontal line and the red curve), which could also reduce the fabrication complexity.

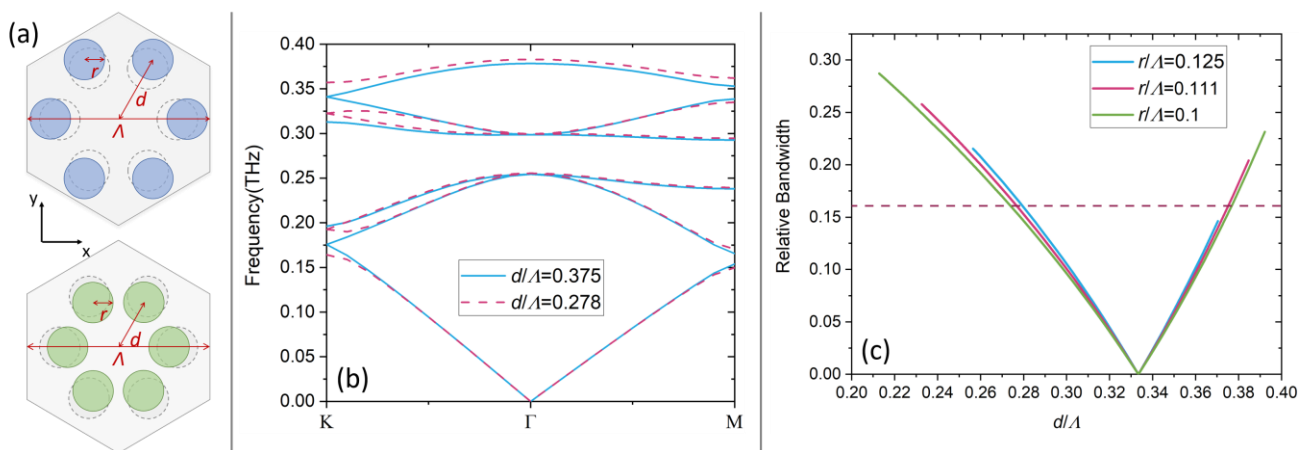


Figure 1. (a) Schematic structures of honeycomb-latticed unit cells, upper: expanded cluster, lower: compressed cluster. (b) Topological bandgap of unit cell where blue solid and red dashed curves represent the modes of expanded and compressed clusters, respectively. (c) Relative bandwidth of topological bandgap as a function of d/Λ for different r/Λ values.

Next, one can assemble the expanded and compressed clusters to achieve an interface that propagates topological pseudospin states, as the red zigzag path shown in Figure 2. Considering a 3D waveguide model, the silicon pillar height, namely the distance between two parallel gold plates, was defined as h (see the inset of Figure 2a). To reveal the effects of structural parameters (including the cluster number on each side of the cladding N_c and the pillar height h) of the topological waveguide on transmission properties, we carry out numerical 3D supercell (shaded region in Figure 2a) simulations. Additionally, we use scattering boundary conditions in the xz -plane of the supercell (shown in Figure 2a) so as to evaluate the lateral confinement. Figure 2b presents the topological band diagram for a waveguide with $N_c = 11$ and $h = \Lambda$. The dashed line in Figure 2b represents the light line. Two modes propagating along either $+x$ (forward) or $-x$ (backward) axes are supported in the topological bandgap range. To present two pseudospin states, we plot the distributions of the x -component of time-averaged power flow (i.e., along the propagation direction) with Poynting vectors (shown as magenta arrows) in Figure 2c where the forward and backward modes exhibit clockwise and anticlockwise spins, respectively. In a nutshell, the two unidirectional topological states have opposite spins; thus, we believe these two modes propagated in a single waveguide path would have negligible crosstalk between each other.

Here, we simulate the topological waveguide supercells with different N_c and h values to optimize the transmission performances, including loss, group velocity dispersion (GVD), and corresponding bandwidth. Figure 3 shows the transmission losses and GVDs of both forward and backward modes for $N_c = 7, 11,$ and 15 while maintaining $h = \Lambda$. The results illustrate that the cluster numbers (N_c above seven) in cladding have minor influences on transmissions except for the loss of backward mode—the low-loss transmission window can be broadened particularly at low frequencies (see Figure 3b). The reason is that the

backward mode propagates at lower frequencies of the topological bandgap, corresponding to a larger mode size than that of the forward mode, which can be better confined in the lateral direction with wider cladding. Moreover, we should note that the GVD curves of both modes have high slopes, because of a huge index contrast between the air region and the high-index pillars—the mode power is partially distributed in pillars, as shown in Figure 2c. Nevertheless, we can still find zero GVD frequencies for both modes, which would achieve high data rate transmission [35].

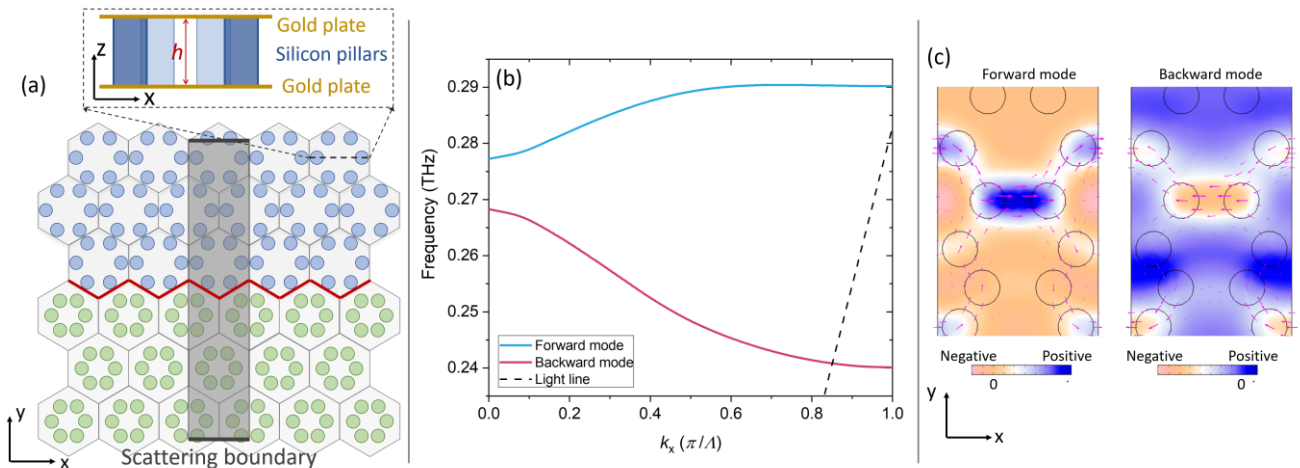


Figure 2. (a) Schematic of the topological waveguide in xy -plane where the shaded region represents the supercell for numerical modeling, the red zigzag path shows topological propagation path, and the inset presents schematic of a honeycomb lattice in xz -plane. (b) Band diagram of the forward (blue curve) and backward (red curve) modes, and the dashed line represents the light line. (c) x -component of time-averaged power flow distributions of the forward and backward modes, and the magenta arrows indicate Poynting vectors where the size of the arrow indicates the strength of vector field.

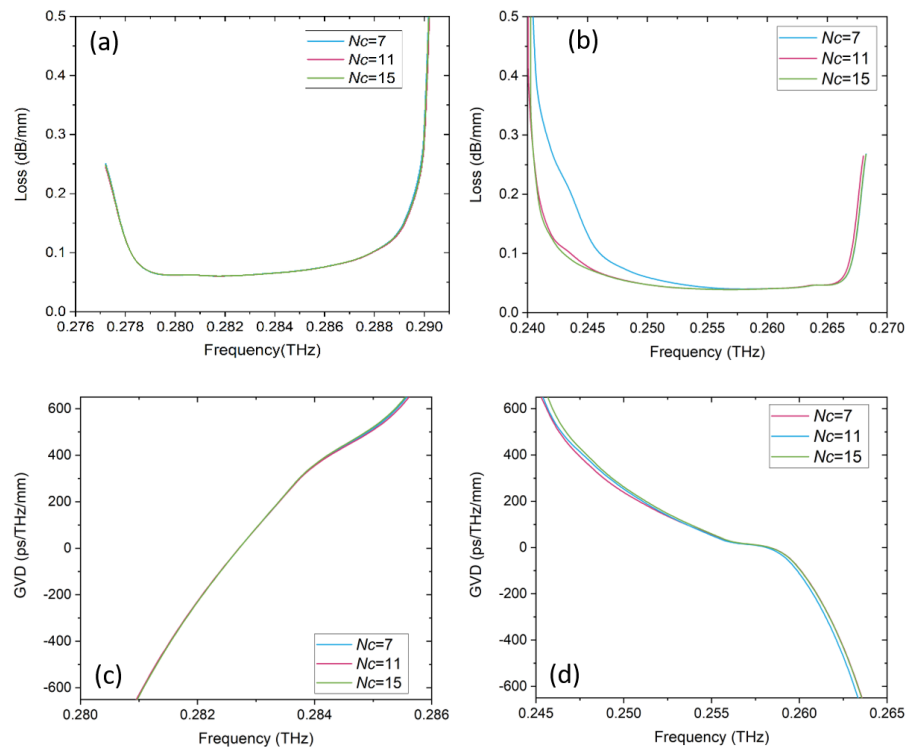


Figure 3. Losses as a function of frequency for (a) forward and (b) backward modes, and GVDs as a function of frequency for (c) forward and (d) backward modes for different N_c values.

We investigate the effect of h values on the supercell simulations of topological waveguides. Here, N_c was fixed at 11, and h values were 0.8Λ and 1.2Λ . The results are shown in Figure 4. Thanks to a large plate separation, a smaller portion of propagating wave power was suffered from the Ohmic loss of the metal surface when $h = 1.2 \Lambda$ for both forward and backward modes, as shown in Figure 4a,b. Nevertheless, it is worth noting that the silicon pillar height was restricted from the silicon-based microfabrication technique because the high aspect ratio pillars would significantly improve the fabrication complexity. From the GVD curves presented in Figure 3c,d, we observe that the waveguide GVDs are independent of N_c and h since the GVD extracted from the band diagram is determined by the photonic crystal unit cell. To achieve the maximum possible bandwidth with low losses, we finalize the waveguide parameters as follows: $\Lambda = 530 \mu\text{m}$, $r = 0.111 \Lambda$, $d = 0.375 (0.278) \Lambda$, $N_c = 11$, and $h = 1.2 \Lambda$. Under the loss criterion of 0.1 dB/mm , the transmission bandwidths are $0.278\text{--}0.289 \text{ THz}$ (bandwidth of 11 GHz , relative value of 3.9%) and $0.242\text{--}0.267 \text{ THz}$ (bandwidth of 25 GHz , relative value 9.8%) for the forward and backward topological modes, respectively. Although the topological bandgap has a wide relative bandwidth of 16.1% (corresponding to 44 GHz), it could not be entirely occupied— 81.8% of the bandgap was utilized for the two topological mode propagations (total transmission bandwidth of two modes is 36 GHz). Furthermore, the frequencies offering the lowest loss and zero GVD for the two modes are indicated in Figure 4, which will be used for the link budget model later.

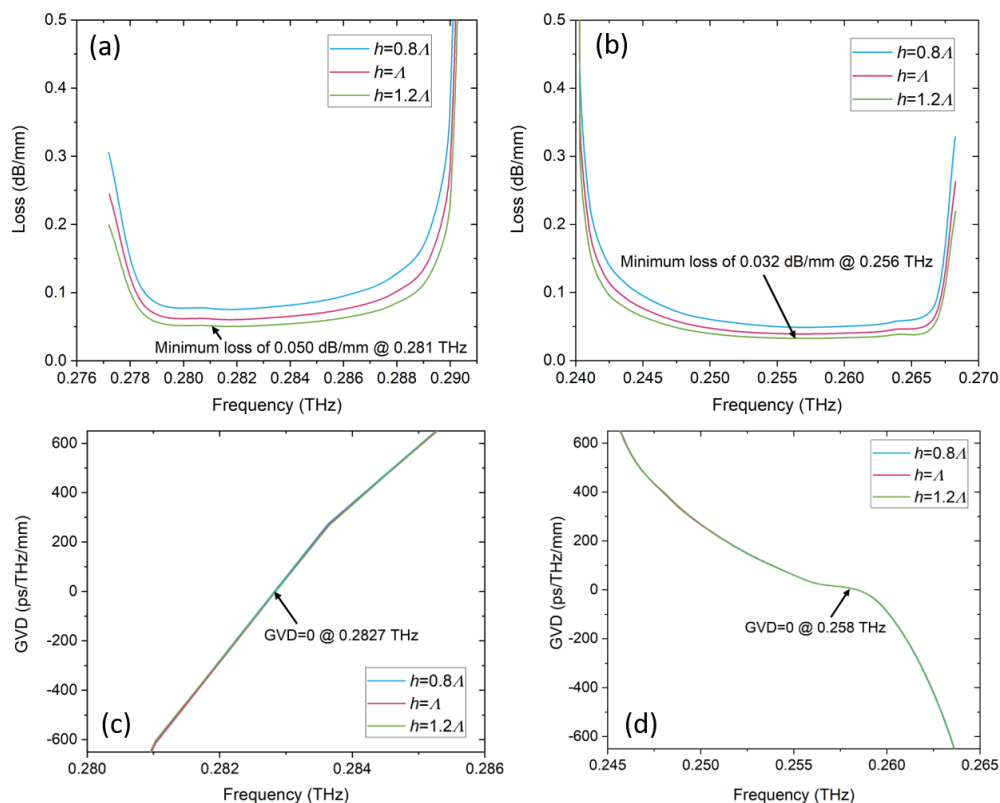
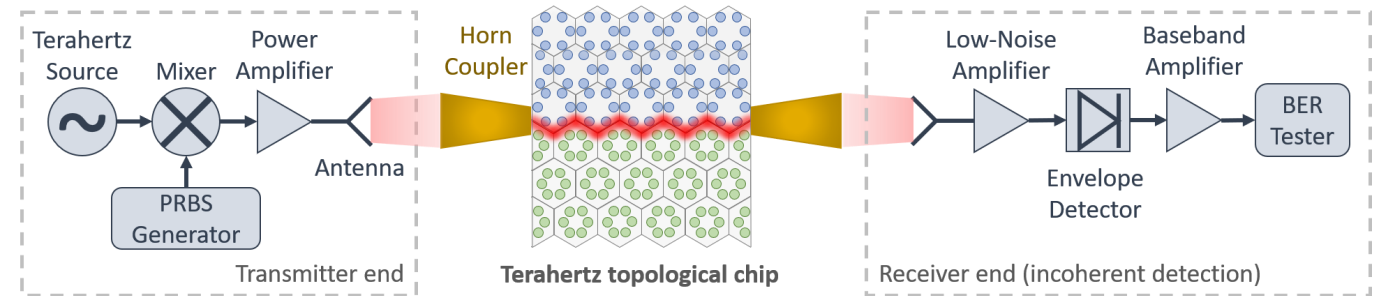


Figure 4. Losses as a function of frequency for (a) forward and (b) backward modes, and GVDs as a function of frequency for (c) forward and (d) backward modes for different h values.

3. Communication Potentials

In this section, we study on-chip communication using the proposed hybrid topological waveguides. An electric-based terahertz wired channel link is modeled here for budget analyses [36]. A schematic diagram of the link as well as corresponding calculations and parameters are presented in Figure 5. At the transmitter end, terahertz carriers can be generated using a voltage-controlled oscillator followed by on-off keying modulation. The

modulated signals are amplified and then launched into the waveguide using an antenna and a horn coupler. Our group recently demonstrated a homemade 3D-printed coupler [37], which can be customized to improve the coupling efficiency. After transmission over the waveguide, another pair of coupler and antenna receives the terahertz radiation. Next, the signals go through a low-noise amplifier for incoherent detection (a peak envelope detector is applied). Finally, the demodulated data is amplified again by a baseband amplifier for signal processing. Using the link budget model, the performance of the baseband signals, including received power (Pr), signal to interference plus noise ratio ($SINR$), and bit error rate (BER), can be evaluated as performed in the left bottom panel of Figure 5. For this on-chip communication link, we assume the generated time-domain terahertz wave has a pulse width of 25 ps, input power of 0 dBm, OOK bit rate of 10 Gbps, and other parameters, for example, the gain and noise factor of amplifiers are shown in the right bottom panel of Figure 5. In the following discussions, we calculate the Pr , $SINR$, and BER for waveguide lengths (L) from 50 mm to 100 mm at four specific carrier frequencies where the forward and backward modes have either the minimum loss or zero GVD (indicated in Figure 4d).



$$S = \frac{1}{T_s} \int_{-T_s/2}^{T_s/2} |s(t)|^2 dt = (G_{LNA} G_{BBA} \sqrt{p_i} G_{PA})^2 e^{-\alpha L} \left(1 + \frac{\beta_2^2 L^2}{T_0^4}\right)^{-\frac{1}{2}} \sqrt{\pi} \frac{T_0'}{T_s} \cdot \text{erf}\left(\frac{T_s}{2T_0'}\right)$$

$$I = \frac{2}{T_s} \int_{T_s/2}^{+\infty} |s(t)|^2 dt = (\sqrt{p_i} G_{PA} G_{LNA} G_{BBA})^2 e^{-\alpha L} \left(1 + \frac{\beta_2^2 L^2}{T_0^4}\right)^{-\frac{1}{2}} \sqrt{\pi} \frac{T_0'}{T_s} \cdot \text{erfc}\left(\frac{T_s}{2T_0'}\right)$$

where $T_0' = \sqrt{T_0^2 + \frac{\beta_2^2 L^2}{T_0^2}}$ is the broadened signal width due to GVD

$$N = \kappa_c \cdot T_{sys} \cdot BW = \kappa_c \cdot \left(\prod_{amp} G_{amp}\right) \cdot (T_{base} + T_{PA} + \frac{T_{LNA}}{G_{PA}} + \frac{T_{BBA}}{G_{PA} G_{LNA}}) \cdot BW$$

where $T_{amp} = T_{base} \cdot (F_{amp} - 1)$ is the effective noise temperature of amplifier

$$Pr = S, \quad SINR = \frac{S}{I + N}, \quad BER_{incoherent} = \frac{1}{2} e^{-\frac{SINR}{4}}$$

Parameter name	Representation Symbol	Default value
Input power	P_i	0 dBm
Characteristic time width of modulation signal	T_0	25 ps
Bit rate	$R_b (1/T_b)$	10 Gbps
Waveguide Loss	α	---
Waveguide GVD	β_2	---
Waveguide length	L	---
Gain of power amplifier	G_{PA}	10 dB
Gain of low-noise amplifier	G_{LNA}	10 dB
Gain of baseband amplifier	G_{BBA}	10 dB
Noise figure of power amplifier	F_{PA}	7 dB
Noise figure of low noise amplifier	F_{LNA}	5 dB
Noise figure of baseband amplifier	F_{BBA}	7 dB
Boltzmann constant	κ_c	---

Figure 5. Top panel: schematic of terahertz waveguide communication link; left bottom panel: calculations of signal power (S), interference (I), noise (N), Pr , $SINR$, and BER ; right bottom panel: parameters used in link budget analyses.

From the results shown in Figure 6, both waveguide loss and GVD contribute to the communication performances. In Figure 6a, all received power Pr values reduce for a longer waveguide because of not only the transmission loss but also the GVD. Considering a Gaussian pulse propagating over a dispersive channel, the GVD leads to pulse broadening while the integral power of the pulse should be constant; thus, the signal power would spread into the interference. From Figure 6b,c, poor performances at a frequency of forward mode with the minimum loss can be significantly observed due to a high GVD magnitude of the mode (603 ps/THz/mm). At other carrier frequencies, the proposed waveguide could support high-SINR, low-BER (below 10^{-3} , which is generally considered to be the forward

error correction (FEC) limit) 10-Gbps on-chip communications over 50–100 mm channel lengths. Comparing the frequencies for the minimum loss and zero GVD, we conclude that for such short links (no longer than 100 mm), the communication performance of the proposed waveguide is largely GVD-dominated. Therefore, it is suggested that frequencies corresponding to near-zero GVDs can be promising carrier candidates in the context of inter/intrachip connection applications. The data rate remains a large scope of enhancement using high-order modulation techniques, such as 16-QAM. Furthermore, the proposed topological chip could support low-crosstalk, full-duplex communications between two nodes thanks to the dual unidirectional topological propagations.

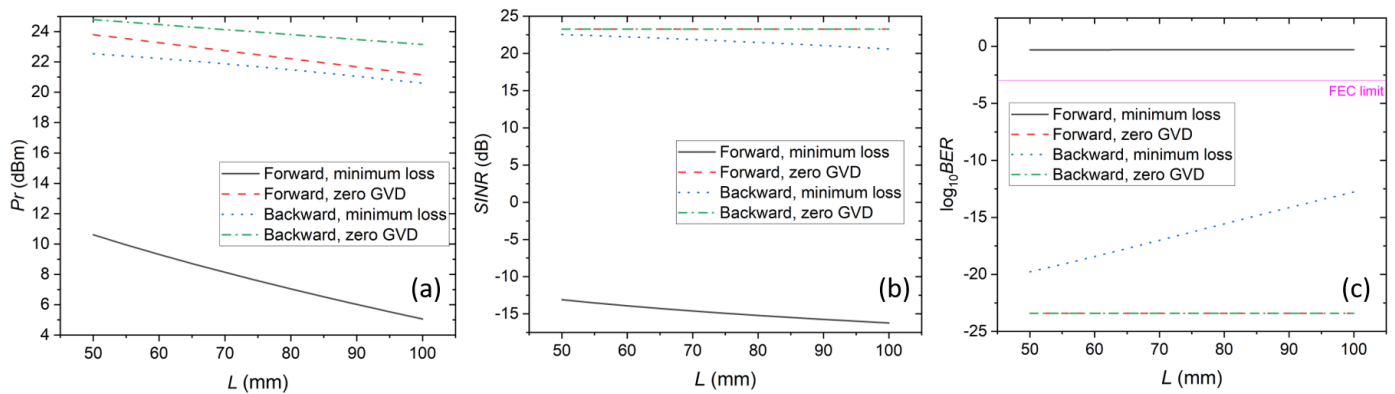


Figure 6. Communication performances (a) P_r , (b) $SINR$, and (c) BER as a function of wavelength length, where black solid, red dashed, blue dotted, and green dash–dotted curves represent carrier frequencies corresponding to forward mode with the minimum loss (frequency at 0.281 THz), forward mode with zero GVD (frequency at 0.2827 THz), backward mode with the minimum loss (frequency at 0.256 THz), and backward mode with zero GVD (frequency at 0.258 THz), respectively. The pink horizontal line indicates the FEC limit ($BER < 10^{-3}$).

4. Conclusions

In summary, we have investigated a hybrid hollow-core topological waveguide for terahertz on-chip communications. The topological bandgap can be widened by improving the deformation of expanded and compressed clusters. Within the bandgap of 16.1% relative bandwidth, two pseudospin modes can be guided along either forward or backward directions. The optimized design shows that the low-loss (below 0.1 dB/mm) bandwidths for forward and backward topological modes are 0.278–0.289 THz and 0.242–0.267 THz, respectively, which occupy 81.8% of the bandgap. We further exploit the proposed waveguide for terahertz on-chip communications. From the link budget analyses, the channel performance is GVD-dependent. At zero GVD frequencies, both forward and backward topological modes can be applied for short-range (50–100 mm) 10-Gbps transmission under the FEC threshold ($BER < 10^{-3}$). Our work demonstrates the possibilities of high-speed on-chip full-duplex interconnection using a single photonic chip, which could be applied to next-generation information systems.

Author Contributions: Conceptualization, H.L.; methodology, H.L.; software, Y.Z. and Y.L.; validation, H.L.; investigation, Y.Z. and Y.L.; resources, H.L. and S.A.; data curation, H.L.; writing—original draft preparation, H.L., Y.Z. and Y.L.; writing—review and editing, S.A.; visualization, Y.Z. and Y.L.; supervision, H.L.; project administration, H.L. All authors have read and agreed to the published version of the manuscript.

Funding: This research was funded by the Fundamental Research Funds for the Central Universities, grant number 2022JBZY004 and the National Natural Science Foundation of China, grant number 62075007.

Data Availability Statement: The data presented in this study may be available from the corresponding author upon reasonable request.

Acknowledgments: S.A. acknowledges the UNSW Scientia Program.

Conflicts of Interest: The authors declare no conflict of interest.

References

1. Kumar, A.; Gupta, M.; Singh, R. Topological integrated circuits for 5G and 6G. *Nat. Electron.* **2022**, *5*, 261–262. [[CrossRef](#)]
2. Xu, G.; Skorobogatiy, M. Wired THz Communications. *J. Infrared Millim. Terahertz Waves* **2022**, *43*, 728–778. [[CrossRef](#)]
3. Holloway, J.W.; Dogiamis, G.C.; Han, R. Innovations in Terahertz Interconnects: High-Speed Data Transport Over Fully Electrical Terahertz Waveguide Links. *IEEE Microw. Mag.* **2020**, *21*, 35–50. [[CrossRef](#)]
4. Sengupta, K.; Nagatsuma, T.; Mittleman, D.M. Terahertz integrated electronic and hybrid electronic–photonic systems. *Nat. Electron.* **2018**, *1*, 622–635. [[CrossRef](#)]
5. Zhang, Y.; Lu, Y.; Yuan, M.; Xu, Y.; Xu, Q.; Yang, Q.; Liu, Y.; Gu, J.; Li, Y.; Tian, Z.; et al. Rotated Pillars for Functional Integrated On-Chip Terahertz Spoof Surface-Plasmon-Polariton Devices. *Adv. Opt. Mater.* **2022**, *10*, 2102561. [[CrossRef](#)]
6. Cao, Y.; Nallappan, K.; Xu, G.; Skorobogatiy, M. Add drop multiplexers for terahertz communications using two-wire waveguide-based plasmonic circuits. *Nat. Commun.* **2022**, *13*, 4090. [[CrossRef](#)] [[PubMed](#)]
7. Atakaramians, S.; Afshar, V.S.; Monro, T.M.; Abbott, D. Terahertz dielectric waveguides. *Adv. Opt. Photonics* **2013**, *5*, 169–215. [[CrossRef](#)]
8. Islam, M.S.; Cordeiro, C.M.B.; Franco, M.A.R.; Sultana, J.; Cruz, A.L.S.; Abbott, D. Terahertz optical fibers [Invited]. *Opt. Express* **2020**, *28*, 16089–16117. [[CrossRef](#)]
9. Li, H.; Atakaramians, S.; Lwin, R.; Tang, X.; Yu, Z.; Argyros, A.; Kuhlmeier, B.T. Flexible single-mode hollow-core terahertz fiber with metamaterial cladding. *Optica* **2016**, *3*, 941–947. [[CrossRef](#)]
10. Withayachumnankul, W.; Fujita, M.; Nagatsuma, T. Integrated Silicon Photonic Crystals Toward Terahertz Communications. *Adv. Opt. Mater.* **2018**, *6*, 1800401. [[CrossRef](#)]
11. Zhu, H.-T.; Xue, Q.; Hui, J.-N.; Pang, S.W. Design, Fabrication, and Measurement of the Low-Loss SOI-Based Dielectric Microstrip Line and its Components. *IEEE Trans. Terahertz Sci. Technol.* **2016**, *6*, 696–705. [[CrossRef](#)]
12. Tsuruda, K.; Fujita, M.; Nagatsuma, T. Extremely low-loss terahertz waveguide based on silicon photonic-crystal slab. *Opt. Express* **2015**, *23*, 31977–31990. [[CrossRef](#)] [[PubMed](#)]
13. Koala, R.A.S.D.; Fujita, M.; Nagatsuma, T. Nanophotonics-inspired all-silicon waveguide platforms for terahertz integrated systems. *Nanophotonics* **2022**, *11*, 1741–1759. [[CrossRef](#)]
14. Headland, D.; Yu, X.; Fujita, M.; Nagatsuma, T. Near-field out-of-plane coupling between terahertz photonic crystal waveguides. *Optica* **2019**, *6*, 1002–1011. [[CrossRef](#)]
15. Gao, W.; Lee, W.S.L.; Fumeaux, C.; Withayachumnankul, W. Effective-medium-clad Bragg grating filters. *APL Photonics* **2021**, *6*, 076105. [[CrossRef](#)]
16. Khanikaev, A.B.; Shvets, G. Two-dimensional topological photonics. *Nat. Photonics* **2017**, *11*, 763–773. [[CrossRef](#)]
17. Price, H.; Chong, Y.; Khanikaev, A.; Schomerus, H.; Maczewsky, L.J.; Kremer, M.; Heinrich, M.; Szameit, A.; Zilberberg, O.; Yang, Y.; et al. Roadmap on topological photonics. *J. Phys. Photonics* **2022**, *4*, 032501. [[CrossRef](#)]
18. Kumar, A.; Gupta, M.; Pitchappa, P.; Wang, N.; Fujita, M.; Singh, R. Terahertz topological photonic integrated circuits for 6G and beyond: A Perspective. *J. Appl. Phys.* **2022**, *132*, 140901. [[CrossRef](#)]
19. Kim, M.; Jacob, Z.; Rho, J. Recent advances in 2D, 3D and higher-order topological photonics. *Light Sci. Appl.* **2020**, *9*, 130. [[CrossRef](#)] [[PubMed](#)]
20. Tang, G.J.; He, X.T.; Shi, F.L.; Liu, J.W.; Chen, X.D.; Dong, J.W. Topological Photonic Crystals: Physics, Designs, and Applications. *Laser Photonics Rev.* **2022**, *16*, 2100300. [[CrossRef](#)]
21. Yang, Y.; Yamagami, Y.; Yu, X.; Pitchappa, P.; Webber, J.; Zhang, B.; Fujita, M.; Nagatsuma, T.; Singh, R. Terahertz topological photonics for on-chip communication. *Nat. Photonics* **2020**, *14*, 446–451. [[CrossRef](#)]
22. Webber, J.; Yamagami, Y.; Ducournau, G.; Szriftgiser, P.; Iyoda, K.; Fujita, M.; Nagatsuma, T.; Singh, R. Terahertz Band Communications With Topological Valley Photonic Crystal Waveguide. *J. Light. Technol.* **2021**, *39*, 7609–7620. [[CrossRef](#)]
23. Kumar, A.; Gupta, M.; Pitchappa, P.; Wang, N.; Szriftgiser, P.; Ducournau, G.; Singh, R. Phototunable chip-scale topological photonics: 160 Gbps waveguide and demultiplexer for THz 6G communication. *Nat. Commun.* **2022**, *13*, 5404. [[CrossRef](#)] [[PubMed](#)]
24. Khan, M.T.A.; Li, H.; Duong, N.N.M.; Blanco-Redondo, A.; Atakaramians, S. 3D-Printed Terahertz Topological Waveguides. *Adv. Mater. Technol.* **2021**, *6*, 2100252. [[CrossRef](#)]
25. Kumar, A.; Gupta, M.; Pitchappa, P.; Tan, Y.J.; Wang, N.; Singh, R. Topological sensor on a silicon chip. *Appl. Phys. Lett.* **2022**, *121*, 011101. [[CrossRef](#)]
26. Liu, X.; Huang, J.; Chen, H.; Qian, Z.; Ma, J.; Sun, X.; Fan, S.; Sun, Y. Terahertz topological photonic waveguide switch for on-chip communication. *Photonics Res.* **2022**, *10*, 1090–1096. [[CrossRef](#)]
27. Yang, Q.; Wang, D.; Kruk, S.; Liu, M.; Kravchenko, I.; Han, J.; Kivshar, Y.; Shadrivov, I. Topology-empowered membrane devices for terahertz photonics. *Adv. Photonics* **2022**, *4*, 046002. [[CrossRef](#)]
28. Xiong, H.; Lu, Y.; Wu, Q.; Li, Z.; Qi, J.; Xu, X.; Ma, R.; Xu, J. Topological Valley Transport of Terahertz Phonon–Polaritons in a LiNbO₃ Chip. *ACS Photonics* **2021**, *8*, 2737–2745. [[CrossRef](#)]

29. Li, H.; Ouyang, C.; Ma, J.; Liu, S.; Liu, Y.; Xu, Q.; Li, Y.; Tian, Z.; Gu, J.; Han, J.; et al. On/Off Switching of Valley Topological Edge States in the Terahertz Region. *IEEE Photonics J.* **2022**, *14*, 4633206. [[CrossRef](#)]
30. Shen, Y.; Ji, J.; Li, H.-C.; Zhang, L.; Yu, X.; Yan, S.-B.; Rasmussen, M.; Shen, Q.; Madhi, D.; Zhou, B.-B.; et al. Realization of Photonic Topological Insulators at Terahertz Frequencies Characterized by Time-Domain Spectroscopy. *Phys. Rev. Appl.* **2022**, *18*, 064025. [[CrossRef](#)]
31. Li, H.; Low, M.X.; Ako, R.T.; Bhaskaran, M.; Sriram, S.; Withayachumnankul, W.; Kuhlmeiy, B.T.; Atakaramians, S. Broadband Single-Mode Hybrid Photonic Crystal Waveguides for Terahertz Integration on a Chip. *Adv. Mater. Technol.* **2020**, *5*, 2000117. [[CrossRef](#)]
32. Wu, L.H.; Hu, X. Scheme for Achieving a Topological Photonic Crystal by Using Dielectric Material. *Phys. Rev. Lett.* **2015**, *114*, 223901. [[CrossRef](#)]
33. Yang, Y.; Xu, Y.F.; Xu, T.; Wang, H.-X.; Jiang, J.-H.; Hu, X.; Hang, Z.H. Visualization of a Unidirectional Electromagnetic Waveguide Using Topological Photonic Crystals Made of Dielectric Materials. *Phys. Rev. Lett.* **2018**, *120*, 217401. [[CrossRef](#)] [[PubMed](#)]
34. Degirmenci, E.; Landais, P. Finite element method analysis of band gap and transmission of two-dimensional metallic photonic crystals at terahertz frequencies. *Appl. Opt.* **2013**, *52*, 7367–7375. [[CrossRef](#)]
35. Nallappan, K.; Cao, Y.; Xu, G.; Guerboukha, H.; Nerguizian, C.; Skorobogatiy, M. Dispersion-limited versus power-limited terahertz communication links using solid core subwavelength dielectric fibers. *Photonics Res.* **2020**, *8*, 1757–1775. [[CrossRef](#)]
36. Wang, Y.; Gao, W.; Han, C. End-to-end Modeling and Analysis for Terahertz Wireline Transmission System with Solid Polymer Fiber. In Proceedings of the ICC 2021—IEEE International Conference on Communications, Montreal, QC, Canada, 14–23 June 2021; pp. 1–6.
37. Wang, Q.; Shah, S.D.A.; Li, H.; Kuhlmeiy, B.; Atakaramians, S. 20 dB improvement utilizing custom-designed 3D-printed terahertz horn coupler. *Opt. Express* **2023**, *31*, 65–74. [[CrossRef](#)]

Disclaimer/Publisher’s Note: The statements, opinions and data contained in all publications are solely those of the individual author(s) and contributor(s) and not of MDPI and/or the editor(s). MDPI and/or the editor(s) disclaim responsibility for any injury to people or property resulting from any ideas, methods, instructions or products referred to in the content.